



## Facile synthesis and electrochemical performance of the nanoscaled FePy<sub>y</sub> anode



Guixin Wang <sup>a, b, \*</sup>, Ruibo Zhang <sup>b</sup>, Tianchan Jiang <sup>b</sup>, Natasha A. Chernova <sup>b</sup>, Zhixin Dong <sup>b</sup>, M. Stanley Whittingham <sup>b, \*</sup>

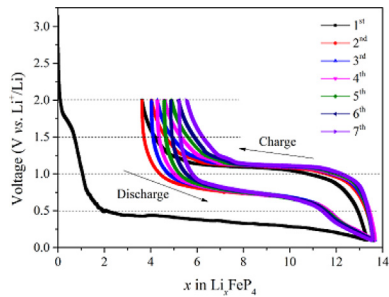
<sup>a</sup> College of Chemical Engineering, Sichuan University, Chengdu 610065, China

<sup>b</sup> Chemistry and Materials, State University of New York at Binghamton, NY 13902-6000, USA

### HIGHLIGHTS

- Nanoscaled FePy<sub>y</sub> anode material with a high phosphorous content has been facilely synthesized.
- The FePy<sub>y</sub> has higher capacity and better cyclability at various rates than the reported results to date.
- The fade mechanism of the FePy<sub>y</sub> was analyzed by different techniques.

### GRAPHICAL ABSTRACT



### ARTICLE INFO

#### Article history:

Received 2 May 2014

Received in revised form

13 July 2014

Accepted 15 July 2014

Available online 23 July 2014

#### Keywords:

FePy<sub>y</sub> alloy

Mechanochemical method

Electrochemical performance

XRD

EIS

### ABSTRACT

Fe–P alloys with high phosphorous content have been targeted as promising anode materials because of their high theoretical capacity. However, the synthesis and cycling performance remain great challenges. Hereby FePy<sub>y</sub> ( $3 \leq y \leq 4$ ) nanoparticles are facilely synthesized through a dry mechanochemical method by reacting iron and red phosphorus powders in an inert atmosphere. The morphology and crystal structure of this material are characterized by SEM and XRD, respectively, while the electrochemical performance is evaluated by a number of different techniques. The 1st and 2nd discharge capacity of FePy<sub>y</sub> reaches 1984 mAh g<sup>-1</sup> and 1486 mAh g<sup>-1</sup>, respectively, and after 10 cycles at 0.03 mA cm<sup>-2</sup> (20 mA g<sup>-1</sup>, 0.03C), the capacity remains 1089 mAh g<sup>-1</sup> with a coulombic efficiency of 97%, much higher than the reported results to date. The cyclability of this material becomes fairly better at a higher current density, but the specific capacity is lower compared to that of the smaller current density. By adding fluorinated ethylene carbonate (FEC) to the electrolyte, the cycling performance of this material was improved. The EIS analysis has also been performed in order to better understand the capacity fade mechanism of FePy<sub>y</sub>.

© 2014 Elsevier B.V. All rights reserved.

### 1. Introduction

With the demand of portable electronic devices and electric vehicles growing, lithium-ion batteries with a higher energy density are attracting more and more attentions from both the fundamental studies and the real-world applications. In addition to the electrolyte and separator, the research community has mainly focused on the novel electrode materials with higher capacity and

\* Corresponding authors. Chemistry and Materials, State University of New York at Binghamton, NY 13902-6000, USA.

E-mail addresses: [guixin66@scu.edu](mailto:guixin66@scu.edu) (G. Wang), [stanwhit@gmail.com](mailto:stanwhit@gmail.com), [stanwhit@binghamton.edu](mailto:stanwhit@binghamton.edu) (M.S. Whittingham).

energy density to satisfy the demand. Among these electrode materials, alloys and intermetallic compounds are promising candidates for energy storage owing to their remarkable advantages [1–5]. Regarding a number of different methods to synthesize these alloys and intermetallic compounds, the mechanochemical method is the first choice and is always being utilized to prepare nanoscale alloys because it's facile, cost-effective and viable for large-scale production.

Elemental phosphorus is interesting for energy conversion and storage purposes since it possesses distinctive physical/chemical properties and electronic structure such as multiple allotropes, a number of oxidation states, and so forth. Phosphorous and its compounds have been utilized to develop novel energy materials with improved performance. Plenty of phosphorous alloys, such as Ti–P [6], V–P [7,8], Mn–P [9,10], Fe–P [11–18], Co–P [19,20], Ni–P [21,22], Cu–P [23,24], Zn–P [25], Ga–P [26], Mo–P [5], In–P [27], Sn–P [28,29], have been reported as the promising anode materials for high performance batteries. Among these alloys, Fe–P alloys are especially interesting because of their unique properties like thermodynamic stability, anti-corrosion ability, high theoretical capacity, environmental compatibility, and low cost. According to the Faradic Law, the theoretical capacity of FeP<sub>4</sub> can reach from 596 to 1787 mAh g<sup>−1</sup> when the lithium-ion transferable number ranges from 1 to 3. However, the large volume change during lithium ion insertion/extraction, electrolyte decomposition, synthesis difficulty, and poor conductivity of FeP<sub>4</sub> prevent its practical application [14,17]. It has been reported that nanostructured materials with specific morphology like porous, layered or tube-like architectures may alleviate the volume change and improve the electrode reaction kinetics [5,18,24]. However, to the best of our knowledge, no report has been made yet for the studies of cycling performance, rate capability and impedance behavior of high phosphorus-content Fe–P alloys (such as FeP<sub>4</sub>).

Herein we report a nanoscaled and high phosphorus-content FeP<sub>y</sub> alloy which can be feasibly synthesized through the mechanochemical method by using common raw materials of iron and red phosphorus powder. The electrochemical performance of this material has been investigated by a number of techniques as well.

## 2. Experimental section

### 2.1. Synthesis of materials

The sample was facilely synthesized by the mechanochemical method in an inert atmosphere. Iron (99.9%, <10 µm, spherical, Alfa Aesar) and red phosphorus (98.5%, 100 mesh, Alfa Aesar) powders were mixed together in a molar ratio of 1:4 (Fe to P) and transferred to a stainless steel can in a glovebox full of helium for ball milling. The weight ratio of stainless steel balls to raw materials is 7.3. The can was sealed and ball milled for 15 h (every 1 h milling with a 30 min break), on a high energy SPEX 8000D dual mixer/mill (SPEX SamplePrep LLC, USA). After being cooled to ambient temperature, the sample was collected for the following characterizations.

### 2.2. Characterization

The phase composition of the as-made material was determined by powder X-ray diffraction (XRD). The data was collected from 15 to 55°, with a step size of 0.02° while spinning the sample to minimize preferred orientation on a Scintag XDS2000 diffractometer equipped with a Ge(Li) solid state detector and a Cu K $\alpha$  sealed tube ( $\lambda$  = 1.54 Å). Synchrotron powder XRD data was collected on the beamline X7B at National Synchrotron Light Source with a wavelength of 0.3196 Å, and quantitatively analyzed by the Rietveld refinement approach using the GSAS/EXPGUI package [30,31]. The

molar ratio of Fe to P was determined by a Varian Vista-MPX axial Inductively Coupled Plasma-Optical Emission Spectroscopy (ICP-OES). The sample was dissolved in a hot aqua regia solution and diluted with high purity water for elemental analysis [15]. The particle size and morphology were characterized using a field emission scanning electron microscope (SEM, ZeissSupra-55). The elemental composition was also analyzed on an energy-dispersive X-ray spectrometry (EDX) by dispersing the sample powders on a silicon wafer using ethanol as the solvent.

### 2.3. Electrochemical evaluation

The as-synthesized powder sample for the electrochemical characterization was mixed well with conductive carbon black and polyvinylidene fluoride (PVDF) binder in a weight ratio of 80:10:10. After adding N-Methyl-2-pyrrolidone (NMP) solvent, the mixture was mechanically homogenized in a stainless steel can to form viscous slurry to coat on a cleaned copper foil using a doctor blade, and the cast thickness was accurately controlled to be 20 µm. After being dried at 80 °C for 12 h, the copper foils loaded with active materials were cut into 1.2 cm<sup>2</sup> wafers which were further dried at ~100 °C under vacuum for ~12 h before using as the working electrodes. Pure lithium foil (thickness ~23 µm, Aldrich) was used as the counter and reference electrodes. The electrochemical performance was evaluated using CR2325 coin cells, which were assembled in a helium-filled glovebox by sandwiching a Celgard 2400 microporous separator between the working electrode and metal lithium. The electrolyte was 1.0 M LiPF<sub>6</sub> dissolved in a mixture of Ethylene Carbonate (EC) and Dimethyl Carbonate (DMC) (1:1 in volume). Electrochemical performances of the above devices were determined between 0.1 V and 2.0 V vs. Li<sup>+</sup>/Li with constant current charge/discharge cycles at 298 K under various current rates. Cyclic voltammetry (CV) tests were conducted in different voltage ranges to obtain the proper working potential, and at different scanning rates to investigate the reaction process. Electrochemical Impedance Spectroscopy (EIS) measurements were carried out at different cycles with a sinusoidal excitation voltage of 10 mV, and the impedance curves were fitted using Zsimpwin and Zview software [32,33]. All electrochemical tests were carried out on a Biologic VMP2 multichannel potentiostat.

## 3. Results and discussion

### 3.1. XRD analysis

The powder XRD patterns of the starting materials and as-synthesized FeP<sub>y</sub> are shown in Fig. 1, exhibiting iron is crystalline with an obvious peak at ~45° while red phosphorus is in amorphous form. Black crystalline powder of FeP<sub>y</sub> is formed after high-energy ball milling for 15 h. Phase identification reveals that this product is composed of FeP<sub>4</sub>, FeP<sub>2</sub> and FeP. A three-phase Rietveld refinement of the synchrotron XRD data is shown in Fig. 2, and the refinement results are summarized in Table 1. The refinement results show that the weight ratio of FeP<sub>4</sub>, FeP<sub>2</sub> and FeP in this material is 49.9%, 17.2% and 32.9%, respectively, suggesting the as-made material is a composite phase comprising different Fe–P alloys. According to the ICP-OES analysis result (Table 2), the molar ratio of P to Fe is 3.8 without dilution and 3.7 with dilution, and the slight excess of Fe can be ascribed to the loss of Fe from the stainless steel balls and can during the ball milling process. It should be pointed out that although we applied the stoichiometric ratio for the starting materials (i.e. the molar ratio of Fe to P is 1:4), it turns out the final product is still a three-phase-mixed composite. It is known that the mechanochemical method utilizes mechanical energy to make a chemical reaction take place, and the reaction

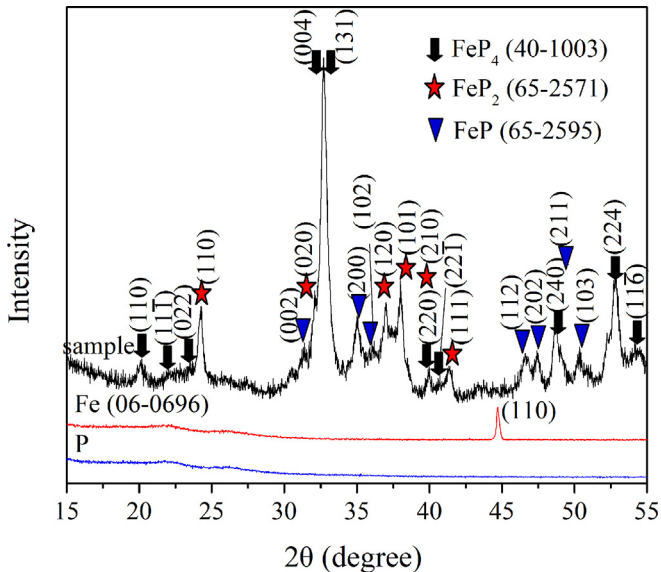


**Fig. 1.** XRD patterns of the starting materials and as-synthesized  $\text{FeP}_y$  (Miller indices and JCPDS numbers of the standard patterns are provided).

process is sometimes complex. Some literature have mentioned that the mechanochemical method can easily create defects (such as dislocations) to afford non-stoichiometric compounds, and the reaction process/mechanism can be material-dependent [7,34–36]. Among iron phosphide alloys, to the best of our knowledge,  $\text{FeP}_4$  single phase has not been synthesized through the mechanochemical method yet, as other impurity phases such as  $\text{FeP}$  and/or  $\text{FeP}_2$  are always found [14,37,38]. This might be due to the partial sublimation of phosphorus during the high energy ball-milling, as well as the special thermodynamic equilibrium achieved by this specific reaction.

### 3.2. Morphology analysis

According to the SEM images in Fig. 3, the  $\text{FeP}_y$  material consists of particles with different size. A large number of small particles (quasi-spherical shape) locate on the surface of big particles; these

**Table 1**  
Composition, unit cell parameters and refinement results of  $\text{FeP}_y$ .

Chemical formula	$\text{FeP}_y$	$\text{FeP}_2$	$\text{FeP}$
Composition	$\text{FeP}_4$	$\text{FeP}_2$	$\text{FeP}$
Crystal system	Orthorhombic	$Pnnm$	$Pna2_1$
Space group	$C222_1$		
$a$ (Å)	5.024(3)	5.338(2)	5.173(3)
$b$ (Å)	9.870(2)	5.820(4)	5.797(4)
$c$ (Å)	5.668(3)	2.959(4)	3.150(2)
$V$ (Å $^3$ )	281.081(2)	91.932(2)	94.438(3)
$R_p$		0.0261	
$R_{wp}$		0.0384	
$R_{F2}$		0.0630	

big particles are actually aggregated by the small particles. Due to the strong collision force of the high energy milling, the size of the smallest particle is even below 20 nm, which might be beneficial for mitigating the volume change during lithium insertion/extraction and thus improve the electrochemical performance [5]. In addition, these small nanoparticles will supply plenty of reaction active sites for lithium ions to enhance the electrode reaction activity. According to the EDX results, Fe and P elements are dominant in the  $\text{FeP}_y$  sample (the small amount of Si and C shown under EDX may come from the Si base and carbon coating layer processed for SEM test). The semi-quantitative analysis of EDX shows that the atomic ratio of P: Fe is ~3.7, matching with the ICP-OES result.

### 3.3. CV analysis

The initial open circuit voltage (OCV) of the fresh coin cell (with  $\text{FeP}_y$  as the active electrode material) is about 3.0 V. CV curves at a scanning rate of 0.01 mV s $^{-1}$  with different scanning potential range are provided in Fig. 4(a) and (b). The reduction peak at ~0.6 V is coupled with the oxidation peak at ~1.2 V, forming a redox couple for lithium-ion insertion/extraction during the discharge/charge process. Within the potential range between 0.01 and 2.5 V, the redox peak intensity decreases gradually during cycling. In addition, no scanning area appears within the potential range of 2.0–2.5 V, indicating that the capacity contribution from this range is very low. Therefore, we changed the scanning potential range to 0.1–2.0 V, as shown in Fig. 4(b). From this figure an obscure

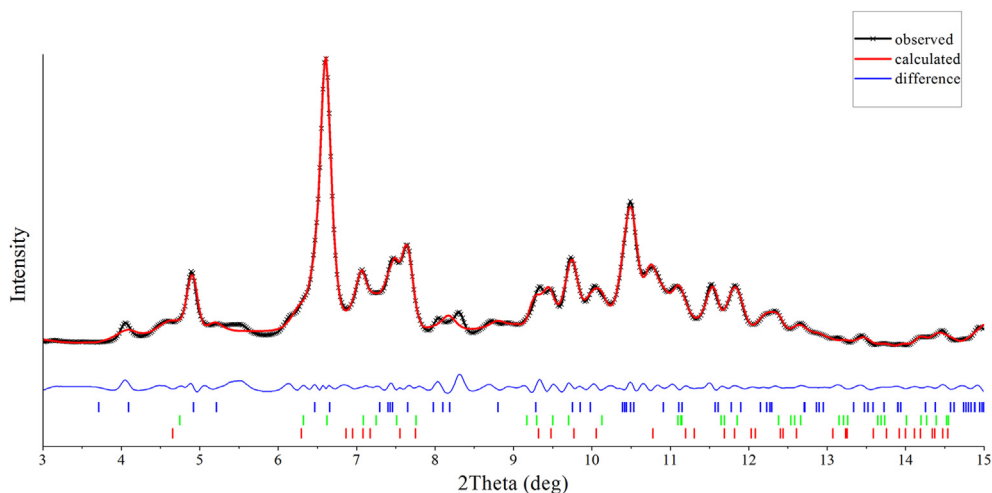


**Fig. 2.** Rietveld refinements of synchrotron X-ray diffraction data of  $\text{FeP}_y$  to identify the phase composition. Red bar:  $\text{FeP}_2$ ; Green:  $\text{FeP}$ ; Blue:  $\text{FeP}_4$ . (For interpretation of the references to colour in this figure legend, the reader is referred to the web version of this article.)

**Table 2**ICP-OES results of the as-synthesized  $\text{FeP}_y$ .

Sample	Fe (ppm)	P (ppm)	Fe/P (in mole)
Blank	0.01525	0.00567	
Undiluted sample	6.54558	13.70780	1 : 3.8
Diluted sample (1:10)	0.66555	1.34182	1 : 3.7

reduction peak can be observed for the 1st cycle while the oxidation peak position is slightly lower than  $\sim 1.2$  V and the intensity is not very high. This may be related to the electrode activation as well as the electrolyte wetting process. The activation continues with the electrochemistry progressing while the electrolyte gradually soaking into the electrode. During the 3rd cycle the reduction peak intensity reaches maximum and then decreases, whereas the maximum intensity of the oxidation peak occurs during the 2nd cycle (and then decreases). The decrease of redox peak intensity possibly suggests a reaction activity decrease, which may be associated with the capacity fade [33,39]. However, the decrease of redox peak intensity between 0.1 and 2.0 V is much lower than that between 0.01 and 2.5 V, therefore, the potential range of 0.1–2.0 V was chosen for the following tests.

### 3.4. Galvanostatic discharge/charge tests

Because Fe–P alloyed anode has a large volume change during the discharge/charge process [17], the loading density of the electrode material will affect its electrochemical performance. Accordingly, four electrodes with different loading weights were prepared to investigate the electrochemical performance. Considering the activation process of the first two cycles, the 3rd galvanostatic discharge/charge cycle curves (current density:  $0.03 \text{ mA cm}^{-2}$ ,  $20 \text{ mA g}^{-1}$ ,  $0.03\text{C}$ ) were chosen and compared in Fig. 5. All these discharge/charge curves exhibit similar shape and charge potential plateaus, however, the capacity and discharge intermediate potential decrease as the loading density of active

materials increases. This indicates a bigger polarization associated with a lower lithium-ion transfer rate as well as more serious disturbance from the volume change in the thicker electrode. Therefore, an electrode loading density of  $\sim 1.4 \text{ mg cm}^{-2}$  was selected to obtain the optimized results.

The discharge/charge curves of  $\text{FeP}_y$  from the first seven cycles are shown in Fig. 6(a). Except for the 1st discharge curve possessing an average potential plateau of  $\sim 0.3$  V, all other curves have a stable discharge and charge plateau at  $\sim 0.7$  and  $\sim 1.1$  V, respectively. Moreover, all these discharge/charge curves (except for the 1st discharge) exhibit a similar shape, which reveals that this material has a similar reversible lithium-ion intercalation/de-intercalation behavior after the initial lithium intercalation. During the 1st discharge, the number of inserted lithium ions is  $\sim 13.3$ , which is higher than 12, the maximum lithium accommodating number of  $\text{FeP}_4$  according to the proposed reaction mechanism [14]. However, the number of removed lithium ions decreases to  $\sim 9.7$  after the 1st charge, and the number of re-inserted lithium ions is similar to this value after the 2nd discharge. The excess discharge capacity during the 1st cycle may be ascribed to the formation of solid electrolyte interphase (SEI) film that usually takes place below 1.0 V vs.  $\text{Li}^+/\text{Li}$  for anode materials [17]; such a SEI film may result in a weak reduction peak, which is consistent with the above CV results. This irreversible capacity loss results in a low Coulombic efficiency ( $\sim 73\%$ ) for the 1st cycle. The subsequent charge/discharge curves change little, with all the discharge curves having two obvious knee points at  $\sim 0.9$  and  $\sim 0.5$  V, along with other two knee points at  $\sim 1.0$  and  $\sim 1.2$  V on the charge curves. Moreover, it can be observed that all the discharge/charge potential plateaus are somewhat inclined, (different from the flat potential plateaus of  $\text{Li}_4\text{Ti}_5\text{O}_{12}$  [40]), implying that the lithium-ion insertion/extraction process of this material behaves as a single phase-type reaction.

Fig. 6(b) shows the galvanostatic discharge/charge curves of  $\text{FeP}_y$  at different current densities from the 3rd cycle. With the current density increasing from  $0.03$  to  $0.3 \text{ mA cm}^{-2}$ , the amount of lithium reacting decreases from 9.7 to 0.5, and it returns to 2.0

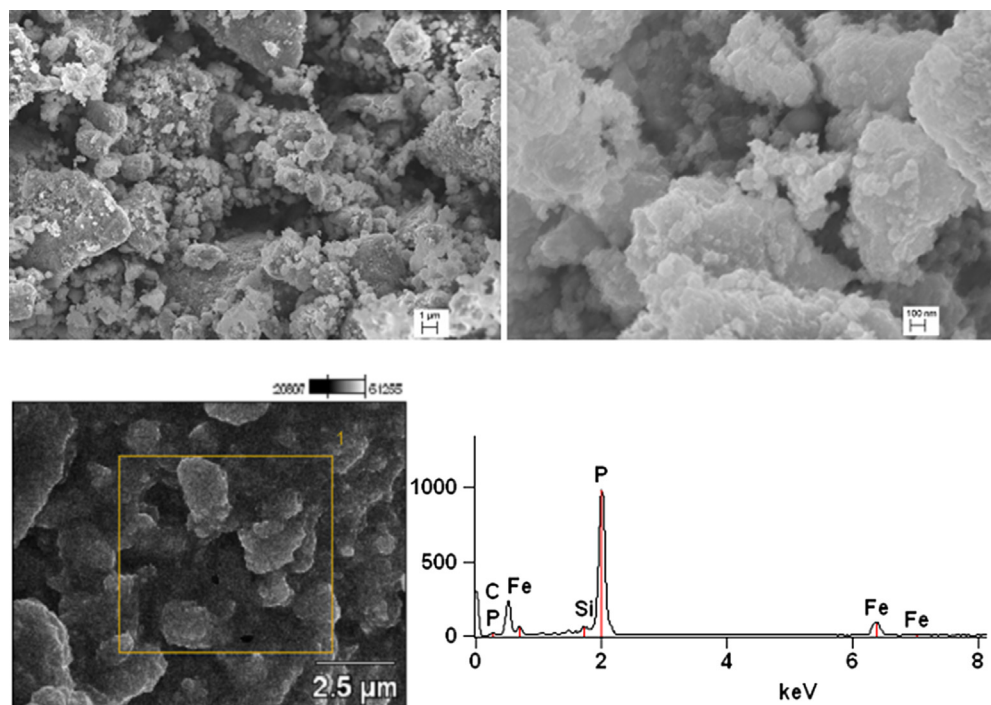


Fig. 3. SEM images and EDX analysis of the as-synthesized  $\text{FeP}_y$ .

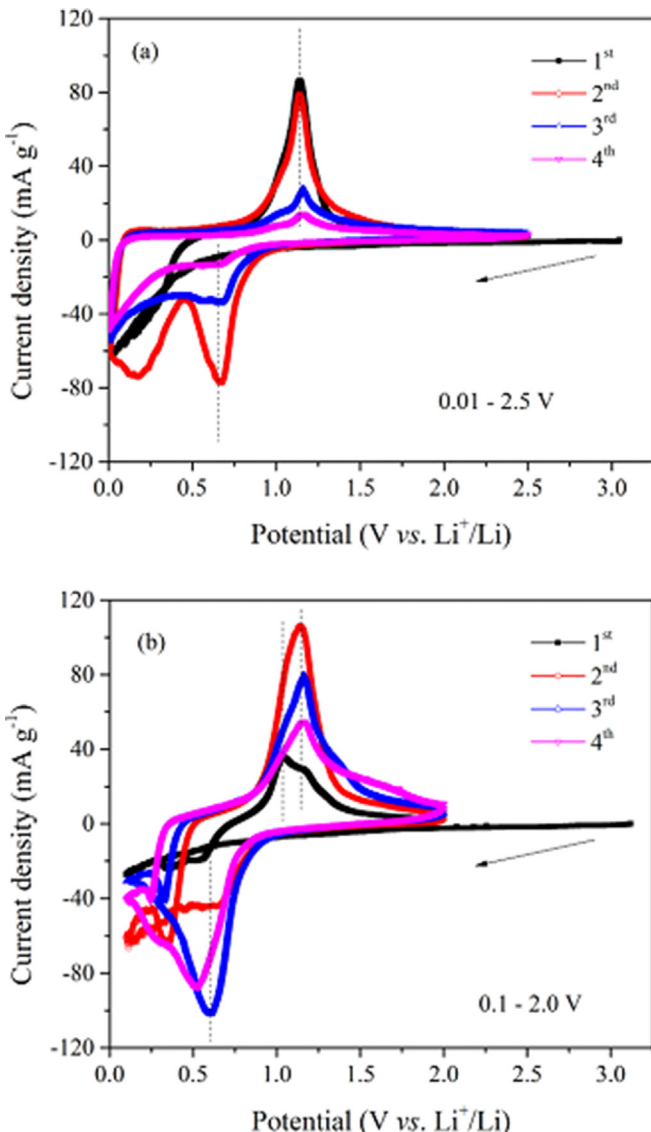


Fig. 4. CV curves of FePy at a scanning rate of  $0.01 \text{ mV s}^{-1}$  with different scanning windows (a) 0.01–2.5 V and (b) 0.1–2.0 V.

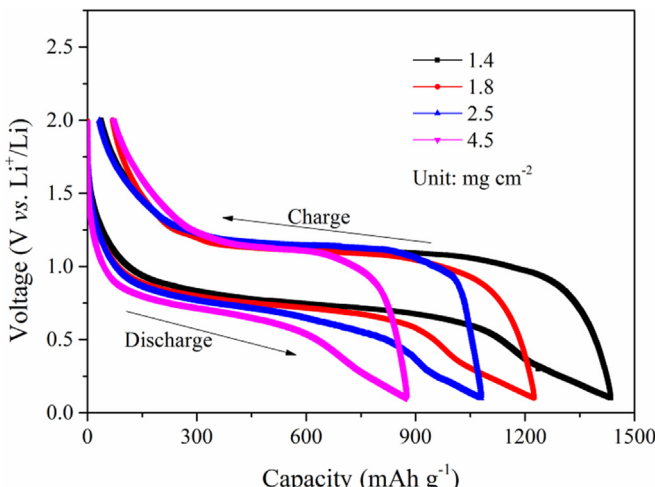


Fig. 5. Comparison of electrode loading density on the 3rd cycle discharge/charge curves.

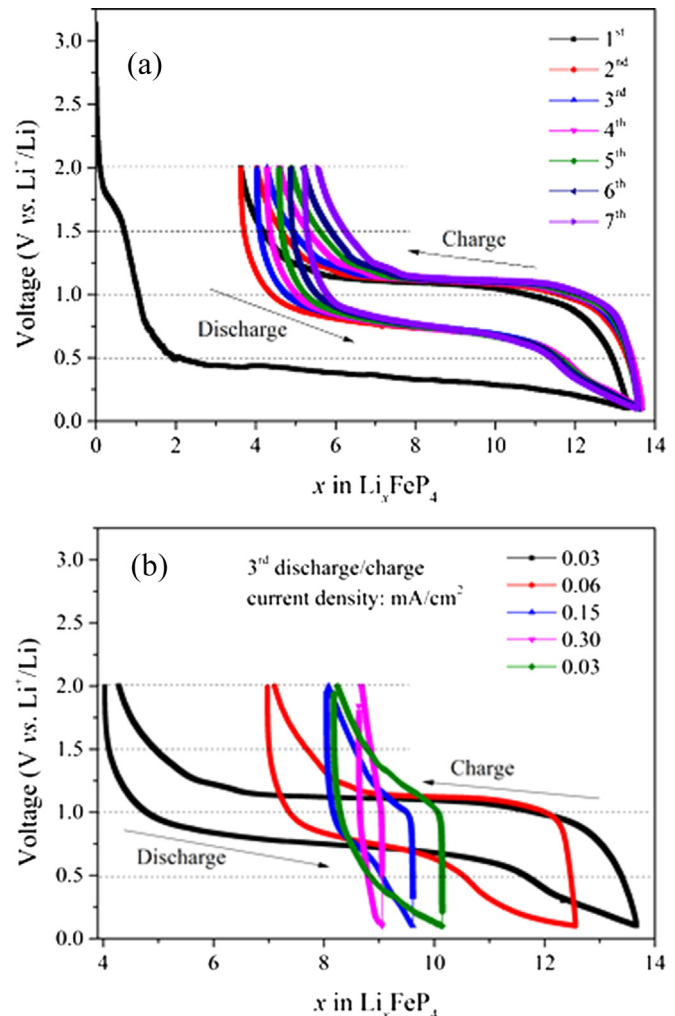
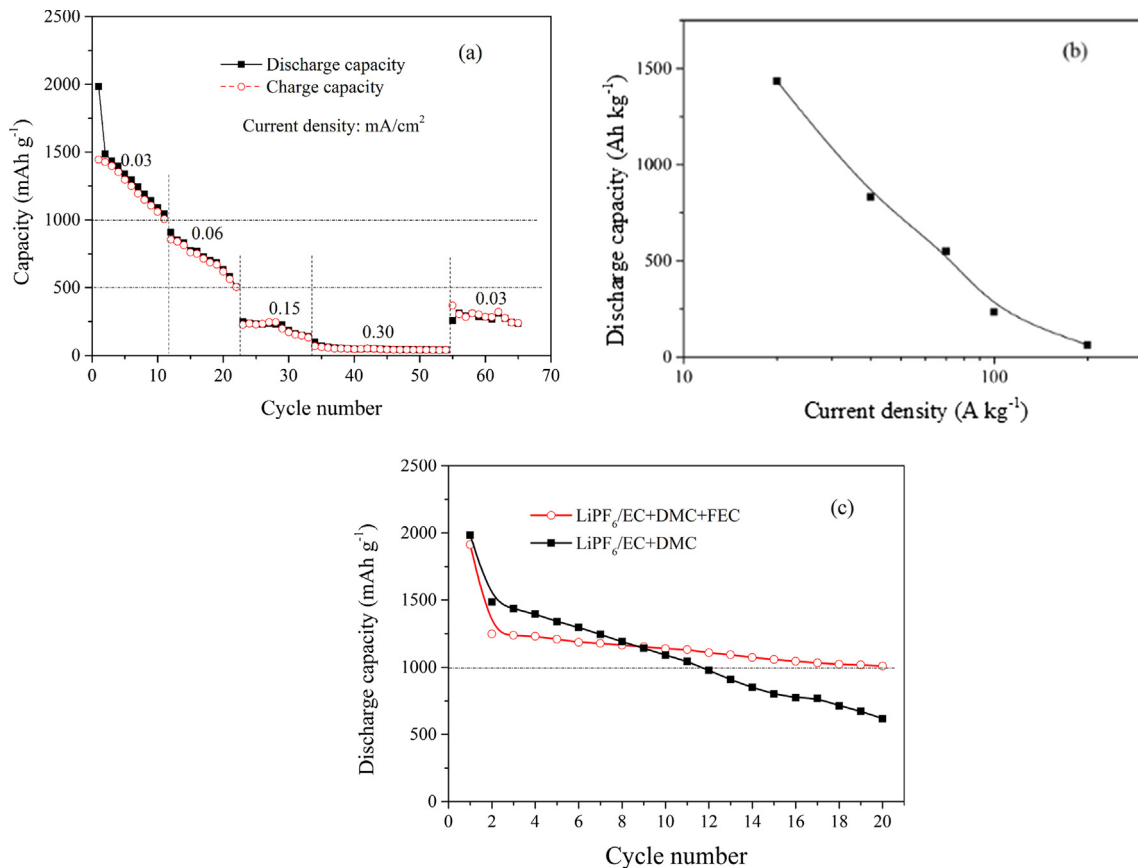


Fig. 6. Galvanostatic discharge/charge curves of the as-synthesized FePy sample at (a) a constant current density of  $0.03 \text{ mA cm}^{-2}$  from the first seven cycles; and (b) current densities of 0.03, 0.06, 0.15, 0.30, and then back to  $0.03 \text{ mA cm}^{-2}$ , respectively, from the 3rd cycle.

when the current density back to  $0.03 \text{ mA cm}^{-2}$ . This shows a slow kinetic behavior of this material, and that may be related to its low conductivity as well as the difficulty of building the new structures.

To the best of our knowledge, there is no report about the cyclability or rate performance of high phosphorus-content iron phosphide anodes. Therefore, we investigated the cycling and rate performance of FePy at different current densities (Fig. 7). As we mentioned above, because the 1st discharge capacity of this material always contains contributions from side reactions such as SEI formation, we chose the 2nd cycle (stabilized) capacity as the reference point for the cycling retention study. As shown in Fig. 7(a), at the current density of  $0.03 \text{ mA cm}^{-2}$  (0.03C), the reversible discharge capacity of FePy remains  $\sim 1089 \text{ mAh g}^{-1}$  after 10 cycles, approximately 73% of the 2nd cycle capacity (55% of the 1st cycle capacity). When the current density increases to  $0.06 \text{ mA cm}^{-2}$ , after 10 cycles the discharge capacity decreases from 908 to  $581 \text{ mAh g}^{-1}$ . It decreases still further when the current density is increased to 0.15 or  $0.30 \text{ mA cm}^{-2}$ , but the cycling behavior becomes stable. When the current is decreased back to  $0.03 \text{ mA cm}^{-2}$  the capacity increases to  $314 \text{ mAh g}^{-1}$ . The coulombic efficiency, except  $\sim 73\%$  for the 1st cycle, remains  $\sim 97\%$  (at the current density of  $0.03 \text{ mA cm}^{-2}$ ) or even higher (at other current densities of  $0.06\text{--}0.30 \text{ mA cm}^{-2}$ ). The key values of discharge capacity and



**Fig. 7.** (a) Cycling and rate performance of FeP<sub>y</sub> (at different current densities of 0.03, 0.06, 0.15, 0.30, and then back to 0.03 mA cm<sup>-2</sup>), (b) Ragone plot, and (c) improved cycling performance by adding FEC as the electrolyte additive.

coulombic efficiency at different current densities are summarized in Table 3. The Ragone plot based on the 3rd cycle discharge capacities (under aforementioned different current densities) is shown in Fig. 7(b). The 3rd discharge capacity can reach up to 1436 Ah kg<sup>-1</sup> when the current density is 20 A kg<sup>-1</sup>, but it decreases to 62 Ah kg<sup>-1</sup> when the current density increases to 200 A kg<sup>-1</sup>. Therefore, this material has a higher energy density than graphene (or doped graphene) [41], Li<sub>4</sub>Ti<sub>5</sub>O<sub>12</sub> [42] and nano

SnO<sub>2</sub>/V<sub>2</sub>O<sub>5</sub> as the anodes [43], whereas its power density needs to be further improved for future applications.

As shown in Fig. 7(a), the capacity fading of FeP<sub>y</sub> needs to be reduced in order to get a better cyclability. It is known that additives such as fluoroethylene carbonate (FEC) can improve the cycling performance of LiMn<sub>2</sub>O<sub>4</sub>/graphite cells [44–46]. Therefore, we tested the cycling performance of FeP<sub>y</sub> by adding 10 wt.% FEC to the pristine electrolyte of 1.0 M LiPF<sub>6</sub>/EC:DMC (1:1 in volume), and the results obtained are shown in Fig. 7(c). After 20 cycles at 0.03 mA cm<sup>-2</sup>, the capacity of FeP<sub>y</sub> is ~1000 mAh g<sup>-1</sup>, which means the capacity retention increases ~22% by adding FEC additive to the electrolyte, much better than the one without FEC. Also, the cycling stability is obviously improved even though the 1st cycle irreversible capacity loss increases a bit. Such an improvement of cyclability may be attributed to adding FEC can benefit the SEI formation and stabilization. In addition, other approaches, such as nanosizing the particle along with morphology control [5,7,18,24,47–49], surface modification with Sn/SnO [16], ZnO [50] or organic carbon [21,51], doping [52], alloying [53], binder modification [54], could also improve the rate performance and cycle stability.

### 3.5. EIS analysis

In order to better understand the electrode reaction and capacity fade mechanism of FeP<sub>y</sub>, EIS measurements were carried out on the electrodes at different state of discharge: one fresh cell with others discharging to 1.0 V, 0.5 V, and 0.1 V, respectively. They are denoted as “1D1.0V” (1st cycle, discharged to 1.0 V),

**Table 3**  
Summary of the cycle performance of FeP<sub>y</sub>.

Current density and the cycle number	Discharge capacity (mAh g <sup>-1</sup> )	Coulombic efficiency (%)
0.03 mA cm <sup>-2</sup>		
1st	1984	73
2nd	1486	96
10th	1089	97
0.06 mA cm <sup>-2</sup>		
2nd	850	99
10th	581	98
0.15 mA cm <sup>-2</sup>		
2nd	236	99
10th	149	98
0.30 mA cm <sup>-2</sup>		
2nd	69	98
10th	50	99
20th	41	99
0.03 mA cm <sup>-2</sup>		
2nd	314	97
10th	244	99

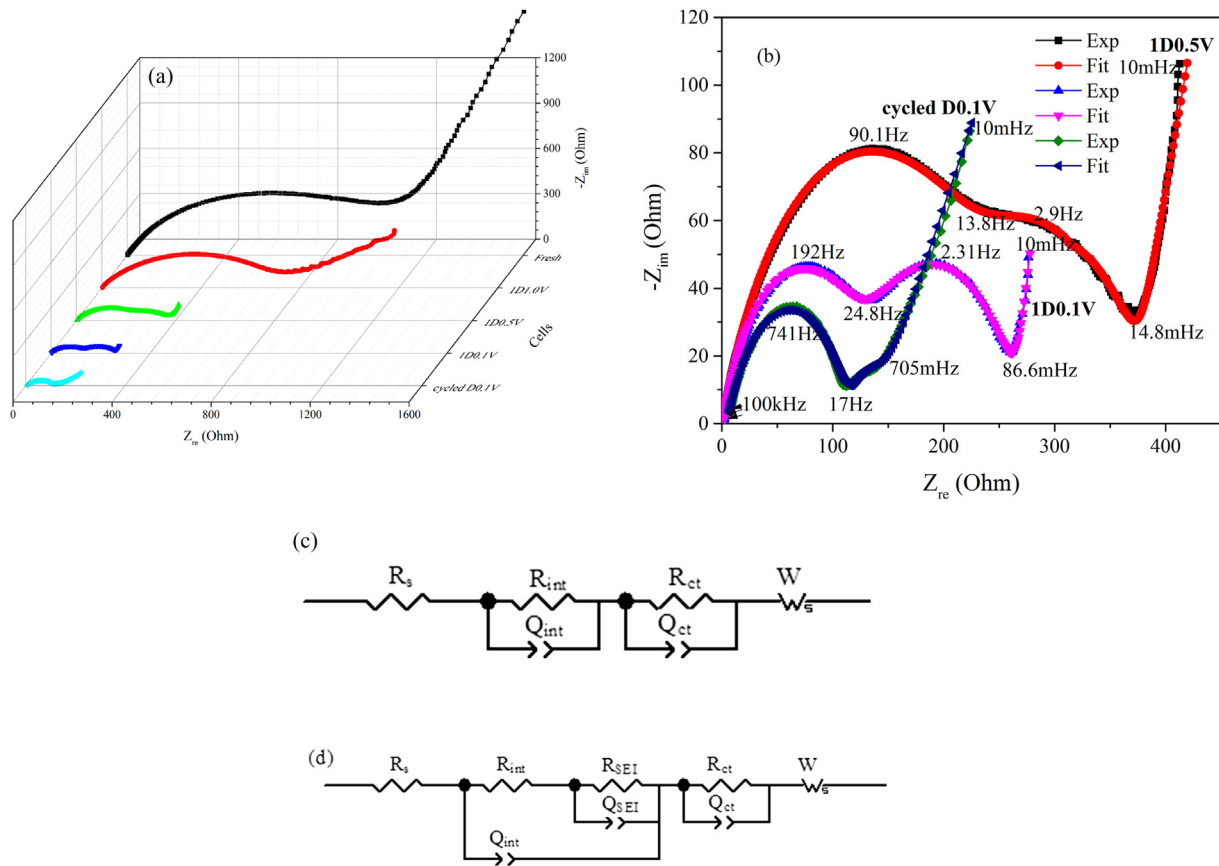


**Fig. 8.** (a) EIS curves of FePy at different state of discharge, (b) EIS fitting results, (c) the equivalent circuit model without SEI component and (d) the equivalent circuit model with SEI component.

“1D0.5V” (1st cycle, discharged to 0.5 V), “1D0.1V” (1st cycle, discharged to 0.1 V), and “cycled D0.1V” (66th cycle, discharged to 0.1 V), respectively. The Nyquist plots, along with the corresponding equivalent circuit models for EIS data fitting, are presented in Fig. 8. Obviously, their shapes are greatly different from each other. For the fresh cell (with OCV of 3.0 V), the EIS curve consists of a depressed semicircle in the high-to-medium frequency region and an oblique line with a slope of ~1 in the low frequency region. When the cell is discharged to 1.0 V, the semicircle becomes smaller, indicating the interface resistance and charge transfer reaction resistance decrease as the lithium ions inserting into the material. When discharging to 0.5 V, the semicircle splits into two depressed ones, which become more obvious when the potential reaches 0.1 V, similar to that of the discharged Si/C composite anode [55]. As shown in Fig. 8(b), after 65 cycles the 2nd semicircle becomes much weaker despite at the same discharge potential of 0.1 V, indicative of a different electrode reaction process before and after cycling.

Considering the galvanostatic discharge curves, the discharge potential plateaus are all above 0.5 V except for the 1st cycle, suggesting the SEI film formed below 1.0 V [17]. Accordingly, two different models provided in Fig. 8(c) and (d) were adopted to fit the experimental curves with and without the contribution from the SEI resistance. Taking into account of the non-homogeneity such as porosity, roughness and localized distribution in the system, constant phase element  $Q$  is used to represent the capacitance in the models, and a depressed semicircle (Core-Element) will appear when  $Q$  is placed parallel to a resistor. The intercept of the curve on the  $Z'$  axis in the high-frequency region is related to the ohmic resistance of the solution. The semicircles in the high

frequency region are attributed to the SEI formation, or interfacial resistance, or these two combined dependent upon the discharge state [55,56]. The semicircle in the medium frequency region is associated with the charge transfer reaction resistance, and the oblique line in low frequency region can be ascribed to Warburg impedance which is considered as the semi-infinite chemical diffusion of lithium ions in the bulk electrode.

The experimental curves can be fitted well by using the models of  $R_s(Q_{int}R_{int})(Q_{ct}R_{ct})W$  and  $R_sQ_{int}(R_{int}(Q_{SEI}R_{SEI}))(Q_{ct}R_{ct})W$  with ZsimpWin and Z-view softwares, and the fitting parameters are summarized in Table 4. In the equivalent circuit,  $R_s$ ,  $R_{int}$ ,  $Q_{int}$ ,  $R_{SEI}$ ,  $Q_{SEI}$ ,  $R_{ct}$ ,  $Q_{ct}$ , and  $W$  refer to the solution Ohmic resistance (including the contributions from electrolyte, electrode, current collector, etc.), the interfacial resistance (between active material and other adjacent substances such as current collector, conductive additive and binder), SEI resistance, the constant phase element of the SEI, the constant phase element of the interface, the charge transfer reaction resistance, the double-layer capacitance (around active material particles), and the general Warburg impedance, respectively.

**Table 4**  
Fitting of the impedance plots.

Cell	$R_s$ (Ohm)	$R_{int}$ (Ohm)	$R_{SEI}$ (Ohm)	$R_{ct}$ (Ohm)	$W$ (Ohm $s^{-1/2}$ )
Fresh	2.6	1027.1	—	20,139	561.7
1D1.0 V	2.1	658.5	—	52.6	117.9
1D0.5 V	1.9	250.6	68.6	22.1	21.6
1D0.1 V	1.3	156.9	110.7	90.8	10.3
Cycled D0.1 V	5.1	109.7	8.7	14.5	22.3

As for the EIS models of intercalation reaction materials like LiFePO<sub>4</sub> [32] or Li<sub>4</sub>Ti<sub>5</sub>O<sub>12</sub> [57], the  $R_{ct}$  and W share one Q because the charge transfer reaction takes place during the ion diffusion process. However, the W is here connected with other resistance elements sequentially, and  $R_{ct}$  has a separate constant phase element Q of reaction interface, indicating the charge transfer reaction and the ion diffusion take place separately. This is because the FeP<sub>y</sub> alloy would store energy through a conversion reaction. For the conversion reaction, the charge transfer reaction usually takes place at the interface between active material and electrolyte, independent of the ion diffusion process.

After 65 cycles, the semicircle from the charge transfer reaction becomes weak, indicating a decrease of conversion reaction activity. Compared to the “1D0.1V” cell, the solution ohmic resistance  $R_s$  and Warburg diffusion impedance W of the “cycled D0.1V” cell have increased a lot, suggesting lithium-ion diffusion becomes difficult after cycling, meanwhile, the interface resistance  $R_{int}$ , SEI film resistance  $R_{SEI}$  and charge transfer reaction resistance  $R_{ct}$  have decreased, indicating a reduced reaction depth of the SEI film and electrode. Therefore, the semicircle decrease after 65 cycles might be associated with the SEI film breaking down during cycling, which has been demonstrated to be significant important for the cyclability of anode materials [58]. Therefore, such a SEI breakdown during cycling may be one of the key reasons for the capacity fading of this material.

#### 4. Conclusions

In summary, nanoscaled FeP<sub>y</sub> ( $3 < y < 4$ ) material has been successfully synthesized by a facile mechanochemical method using common raw materials of Fe and red P powders in an inert atmosphere. The smallest particle size is below 20 nm, and small particles aggregate into big microsized particles. FeP<sub>y</sub> can be cycled reversibly, which may be due to its nanoscaled particles can reduce the volume change during the discharge/charge process and stabilize the electrochemical reaction. Although there is a capacity loss during the 1st cycle associated with the electrode activation and SEI formation, the 2nd and 3rd discharge capacities can reach 1486 and 1436 mAh g<sup>-1</sup>, respectively. A capacity of 1089 mAh g<sup>-1</sup> (~73.3% of the 2nd cycle capacity, 55% of the 1st cycle capacity) can be delivered after 10 cycles at a current density of 0.03 mA cm<sup>-2</sup>, with the corresponding coulombic efficiency of ~97%. By adding fluoroethylene carbonate (FEC) to the electrolyte, the cycling performance of this material can be improved. Due to the composition complexity of this three-phase composite, as well as the amorphous feature of its lithiated products, the detailed reaction mechanism study of FeP<sub>y</sub> is still underway. Actually there is still a debate about the real reaction mechanism of high phosphorus-content FeP<sub>y</sub> (such as FeP<sub>4</sub>). Does it completely go through an intercalation reaction (FeP<sub>y</sub> + xLi<sup>+</sup> - Li<sub>x</sub>FeP<sub>y</sub>), a conversion reaction (FeP<sub>y</sub> + 3yLi<sup>+</sup> - yLi<sub>3</sub>P + Fe), or these two combined? A conclusive answer is still missing, either because of the amorphous phases formed (which XRD does not see), or because of an unknown lithiated phase, i.e., Li<sub>x</sub>FeP<sub>y</sub>, which was proposed based on the “similar” compound Li<sub>7</sub>MnP<sub>4</sub>, while the structure of Li<sub>x</sub>FeP<sub>y</sub> is still unknown [14]. Therefore, synchrotron-based studies such as pair-distribution function (PDF) analysis (which is a particularly powerful tool to probe the amorphous phase), are needed to determine the detailed reaction mechanism of this material, as well as the key factors that govern the capacity fading. This will help to improve the stability and rate performance of high phosphorus-content Fe-P alloys as the new anode materials for next generation of lithium ion batteries.

#### Acknowledgments

Guixin Wang gratefully acknowledges the National Natural Science Foundation of China (Grant No.21206099) and the China Scholarship Council. This research is supported by DOE-EERE-BATT, DE-AC02-05CH11231 under Award Number 6807148, and by NYSERDA, Award number 18500.

#### References

- [1] J.-M. Tarascon, M. Armand, *Nature* 414 (2001) 359–367.
- [2] M.S. Whittingham, *MRS Bull.* 33 (2008) 411–419.
- [3] J. Cabana, L. Monconduit, D. Larcher, M.R. Palacin, *Adv. Mater.* 22 (2010) E170–E192.
- [4] S. Carenco, D. Portehault, C. Boissiere, N. Mezailles, C. Sanchez, *Chem. Rev.* 113 (2013) 7981–8065.
- [5] M.G. Kim, J. Cho, *Adv. Funct. Mater.* 19 (2009) 1497–1514.
- [6] W. Sang-Gil, J. Jin-Ho, K. Hansu, K. Min Gyu, L. Churl Kyung, S. Hun-Joon, C. Byung Won, *J. Electrochem Soc.* 153 (2006) A1979–A1983.
- [7] T.N. Lambert, D.J. Davis, S.J. Limmer, M.R. Hibbs, J.M. Lavin, *Chem. Commun.* 47 (2011) 9597–9599.
- [8] F. Gillot, M. Ménétrier, E. Bekaert, L. Dupont, M. Morcrette, L. Monconduit, J.M. Tarascon, *J. Power Sources* 172 (2007) 877–885.
- [9] F. Gillot, L. Monconduit, M.L. Doublet, *Chem. Mater.* 17 (2005) 5817–5823.
- [10] D.C.S. Souza, V. Pralong, A.J. Jacobson, L.F. Nazar, *Science* 296 (2002) 2012–2015.
- [11] D.C.C. Silva, O. Crosnier, G. Ouvrard, J. Greidan, A. Safa-Sefat, L.F. Nazar, *Electrochem. Solid-state Lett.* 6 (2003) A162.
- [12] S. Boyanov, J. Bernardi, F. Gillot, L. Dupont, M. Womes, J.-M. Tarascon, L. Monconduit, M.-L. Doublet, *Chem. Mater.* 18 (2006) 3531–3538.
- [13] S. Boyanov, M. Womes, L. Monconduit, D. Zitoun, *Chem. Mater.* 21 (2009) 3684–3692.
- [14] S. Boyanov, D. Zitoun, M. Ménétrier, J.-C. Jumas, M. Womes, L. Monconduit, *J. Phys. Chem. C* 113 (2009) 21441–21452.
- [15] M. Zhao, G.-X. Wang, X.-L. Li, R. Liu, F. Wang, K.-P. Yan, *Metals Mater. Int.* 16 (2010) 993–999.
- [16] W. Sun, C. Luo, G. Wang, K. Yan, *J. Alloys Compd.* 535 (2012) 114–119.
- [17] J.W. Hall, N. Membreño, J. Wu, H. Celio, R.A. Jones, K.J. Stevenson, *J. Am. Chem. Soc.* 134 (2012) 5532–5535.
- [18] I.-T. Park, H.-C. Shin, *Electrochem Commun.* 33 (2013) 102–106.
- [19] Y.-H. Cui, M.-Z. Xue, Z.-W. Fu, X.-L. Wang, X.-J. Liu, *J. Alloys Compd.* 555 (2013) 283–290.
- [20] D. Yang, J. Zhu, X. Rui, H. Tan, R. Cai, H.E. Hoster, D.Y.W. Yu, H.H. Hng, Q. Yan, *ACS Appl. Mater. Interfaces* 5 (2013) 1093–1099.
- [21] S. Carenco, C. Surcin, M. Morcrette, D. Larcher, N. Mezailles, C. Boissiere, C. Sanchez, *Chem. Mater.* 24 (2012) 688–697.
- [22] Y. Lu, J.-P. Tu, Q.-Q. Xiong, J.-Y. Xiang, Y.-J. Mai, J. Zhang, Y.-Q. Qiao, X.-L. Wang, C.-D. Gu, S.X. Mao, *Adv. Funct. Mater.* 22 (2012) 3927–3935.
- [23] M.C. Stan, R. Kloepsch, A. Bhaskar, J. Li, S. Passerini, M. Winter, *Adv. Energy Mater.* 3 (2013) 231–238.
- [24] M.S. Chandrasekar, S. Mitra, *Electrochim. Acta* 92 (2013) 47–54.
- [25] M.P. Bichat, J.L. Pascal, F. Gillot, F. Favier, *Chem. Mater.* 17 (2005) 6761–6771.
- [26] H. Hwang, M.G. Kim, J. Cho, *J. Phys. Chem. C* 111 (2007) 1186–1193.
- [27] M.D. Gerngross, E. Quiroga-Gonzalez, J. Carstensen, H. Foell, *J. Electrochem Soc.* 159 (2012) A1941–A1948.
- [28] B. Leon, J.I. Corredor, J.L. Tirado, C. Perez-Vicente, *J. Electrochem Soc.* 153 (2006) A1829–A1834.
- [29] Y.U. Kim, C.K. Lee, H.J. Sohn, T. Kang, *J. Electrochem Soc.* 151 (2004) A933–A937.
- [30] B.H. Toby, *J. Appl. Crystallogr.* 34 (2001) 210–213.
- [31] A.C. Larson, R.B. Von Dreele, *General Structure Analysis System, LANSCE*, Los Alamos, New Mexico, 1994. MS-H805.
- [32] H. Kang, G. Wang, H. Guo, M. Chen, C. Luo, K. Yan, *Ind. Eng. Chem. Res.* 51 (2012) 7923–7931.
- [33] F. Huang, Q. Zhao, C. Luo, G. Wang, K. Yan, D. Luo, *Chin. Sci. Bull.* 57 (2012) 4237–4243.
- [34] L.J. Ning, Y.P. Wu, S.B. Fang, E. Rahim, R. Holze, *J. Power Sources* 133 (2004) 229–242.
- [35] Z. Zhang, J. Yang, Y. Nuli, B. Wang, J. Xu, *Solid State Ionics* 176 (2005) 693–697.
- [36] W.Y. Li, L.N. Xu, J. Chen, *Adv. Funct. Mater.* 15 (2005) 851–857.
- [37] E. Bekaert, J. Bernardi, S. Boyanov, L. Monconduit, M.-L. Doublet, M. Ménétrier, *J. Phys. Chem. C* 112 (2008) 20481–20490.
- [38] M. Sugitani, N. Kinomura, M. Koizumi, S. Kume, *J. Solid State Chem.* 26 (1978) 195–201.
- [39] A.J. Bard, L.R. Faulkner, *Electrochemical Methods: Fundamentals and Applications*, Wiley, New York, 1980.
- [40] G. Wang, K. Yan, Z. Yu, M. Qu, *J. Appl. Electrochem.* 40 (2010) 821–831.
- [41] Z.-S. Wu, W. Ren, L. Xu, F. Li, H.-M. Cheng, *ACS Nano* 5 (2011) 5463–5471.
- [42] D.J. Crain, J.P. Zheng, D. Roy, *Solid State Ionics* 240 (2013) 10–18.
- [43] J. Yan, A. Sumboja, E. Khoo, P.S. Lee, *Adv. Mater.* 23 (2011) 746–750.

- [44] M.-H. Ryou, G.-B. Han, Y.M. Lee, J.-N. Lee, D.J. Lee, Y.O. Yoon, J.-K. Park, *Electrochim. Acta* 55 (2010) 2073–2077.
- [45] L. Hu, Z. Zhang, K. Amine, *Electrochim. Commun.* 35 (2013) 76–79.
- [46] Y.-M. Lin, K.C. Klavetter, P.R. Abel, N.C. Davy, J.L. Snider, A. Heller, C.B. Mullins, *Chem. Commun.* 48 (2012) 7268–7270.
- [47] C.-M. Park, K.-J. Jeon, *Chem. Commun.* 47 (2011) 2122–2124.
- [48] J.R. Szczecz, S. Jin, *Energy & Environ. Sci.* 4 (2011) 56.
- [49] Y. Zheng, J. Yang, J. Wang, Y. NuLi, *Electrochim. Acta* 52 (2007) 5863–5867.
- [50] X.-L. Li, G.-X. Wang, K.-P. Yan, R. Liu, *J. Inorg. Mater.* 25 (2010) 877–881.
- [51] X.L. Li, Master thesis of Sichuan University, 2011.
- [52] L. Huang, X.-M. Zheng, Y.-S. Wu, L.-J. Xue, F.-S. Ke, G.-Z. Wei, S.-G. Sun, *Electrochim. Commun.* 11 (2009) 585–588.
- [53] L.H. Hu Ren Zong, Zeng MeiQin, Liu JiangWen, Zhu Min, *Chin. Sci. Bull.* 57 (2012) 4119–4130.
- [54] N. Ding, J. Xu, Y. Yao, G. Wegner, I. Lieberwirth, C. Chen, *J. Power Sources* 192 (2009) 644–651.
- [55] J. Guo, A. Sun, X. Chen, C. Wang, A. Manivannan, *Electrochim. Acta* 56 (2011) 3981–3987.
- [56] M. Gabersek, J. Moskon, B. Erjavec, R. Dominko, J. Jamnik, *Electrochim. Solid-state Lett.* 11 (2008) A170–A174.
- [57] R. Dédryvere, D. Foix, S. Franger, S. Patoux, L. Daniel, D. Gonbeau, *J. Phys. Chem. C* 114 (2010) 10999–11008.
- [58] P. Verma, P. Maire, P. Novák, *Electrochim. Acta* 55 (2010) 6332–6341.